Cutting Edge 2

Ultrashort Electron Beam Generation and Diagnosis by Linear Accelerator

Mitsuru Uesaka, Takahiro Watanabe, and Nasr Hafz

Abstract

A 240-fs 18-MeV electron single bunch was generated and synchronized with a 100-fs 0.3-TW Ti:sapphire laser with the time resolution of 330 fs. We have upgraded and tested four diagnostic tools/methods: a femtosecond streak camera, a coherent transition radiation (CTR) interferometer, a far-infrared polychromator, and a fluctuation method. The subpicosecond synchronization system is used to study radiation chemistry. We are close to experimentally demonstrating that a 10-fs tens-of-megaelectronvolt electron single bunch can be produced by laser plasma acceleration using a 12-TW 50-fs laser. This will enable a pump-and-probe analysis system with a time resolution of tens of femtoseconds to explore the boundary between physics and chemistry.

1. Introduction

Ultrashort-beam science and technology began with the experimental verification of 50-fs (rms) 10-MeV electron multi-bunches[1)] and of a 700-fs 35-MeV single bunch.[2)] The S-band (2.856 GHz) laser-photocathode RF electron gun has generated high-quality femtosecond beams with low emittance (<10 mm mrad),[3,4)] and fourth-generation synchrotron light sources are going to be constructed[5,6)]. They will produce ≈100-fs intense x-ray free electron laser via self-amplified spontaneous emission (SASE) and will make possible dynamic microscopic structural analysis. Several compact inverse Compton hard-x-ray (≈10-keV) sources are also under development,[7)] and picosecond and subpicosecond time-resolved synchronization systems using electron linear accelerators and femtosecond lasers have already been used to study ultrafast radiation chemistry. [8-10)] Furthermore, ultrashort beams of electrons, x rays, and ions can be generated by means of laser plasma acceleration using table-top multiterawatt Ti:sapphire lasers. Ultrafast multibeam pump-and-probe analysis using those lasers and femtosecond electron linear accelerators may be able to detect and visualize the movement of atoms in laser-irradiated GaAs monocrystals. Confirming these time resolutions will require the use of ultrashort-electron-pulse diagnostic tools and methodologies, and here we introduce four: a femtosecond streak camera, a coherent-radiation (CR) interferometer, a far-infrared polychromator, and a fluctuation method. Their resolution and reliability have been crosschecked in detail and confirmed.

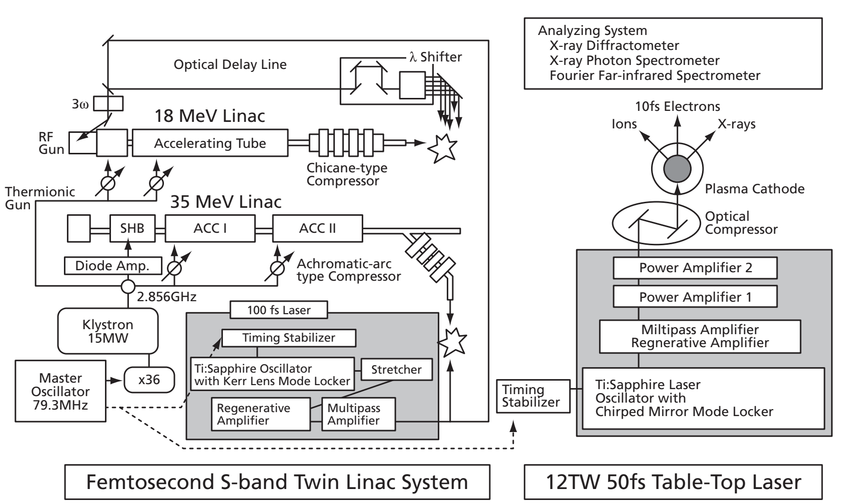

Fig.1 Femtosecond Ultrafast Quantum Phenomena Research Facility.

2. Femtosecond Ultrafast Quantum Phenomena Research Facility

As shown in Fig. 1, the Femtosecond Ultrafast Quantum Phenomena Research Facility at the University of Tokyo's Nuclear Engineering Research Laboratory consists of two S-band electron linear accelerators (linacs), a 0.3-TW 100-fs Ti:sapphire laser, a 12-TW 50-fs Ti:sapphire laser, and equipment for analysis. The linacs are synchronized with the 0.3-TW laser with the time resolution of 330 fs,[11)] and an S-band laser photocathode RF gun developed at Brookhaven National Laboratory (USA)[3)] is installed at the 18 MeV linac. The best beam parameters are an energy of 3 MeV, an emittance of 6 πmm mrad, a pulse width of 10 ps, and a charge per bunch of 7 nC.[12,13)] Using the 12-TW laser, we are performing experiments to generate femtosecond and picosecond pulses of electrons, x rays, ions, and neutrons by means of laser plasma acceleration.

3. Magnetic pulse compression

As shown in Fig. 2, the magnetic pulse

Nuclear Engineering Research Laboratory, University of Tokyo

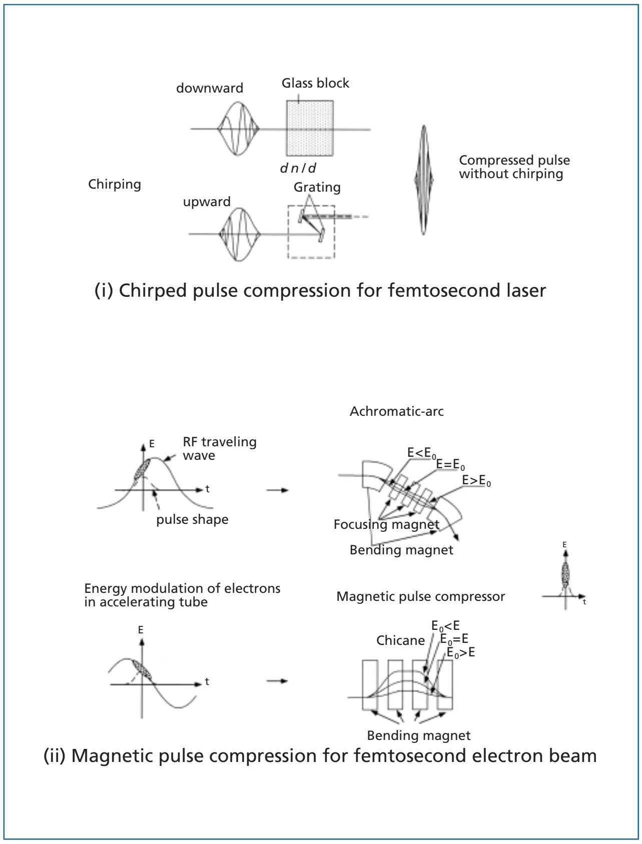

Fig.2 Magnetic pulse compression for electron pulse and chirped pulse compression for laser pulse.

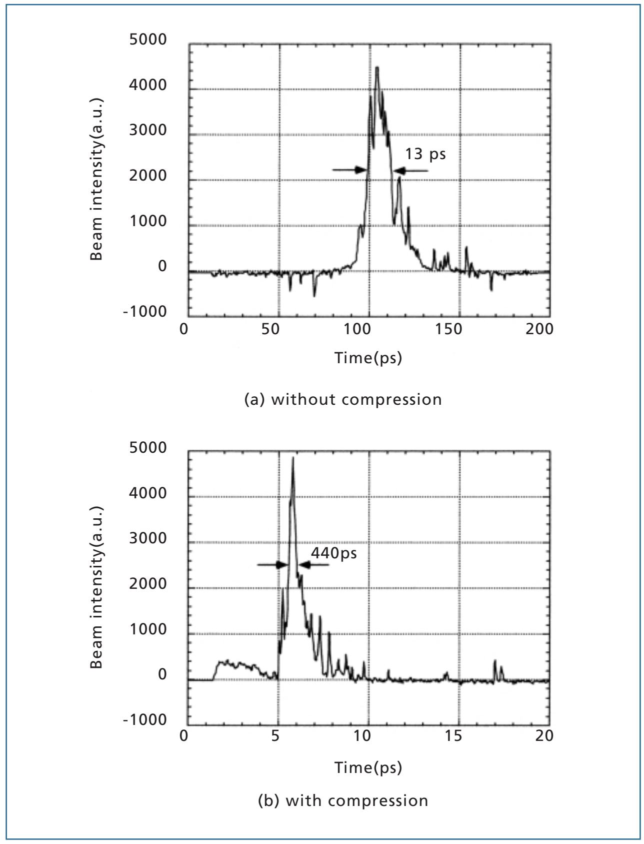

Fig.3 Pulse shapes without and with compression measured by the femtosecond streak camera.

compression used to generate femtosecond electron pulses is analogous to the chirped pulse compression (CPA) in femtosecond lasers. CPA consists of chirping (longitudinal energy modulation), stretching, amplification, and compression. Generally a set of gratings is used for chirping and compression. Higher/lower-energy photons are located in an earlier/later part of laser pulse for downward/upward chirping. If we replace photons with electrons, chirping and compression become magnetic pulse compression. Downward and upward chirping are respectively done by putting the electron beam on an increasing or decreasing RF phase of the accelerating traveling wave in an accelerating tube. Then the beam passes through a magnet assembly consisting of bending and focusing magnets. The chirping is transformed to path-length modulation because the bending radius is inversely linear to the electron energy. Therefore the later electrons can catch up with the earlier electrons and the beam is compressed. At the 35-MeV linac we have an achromatic-are-type compressor for downward chirping, and at the 18-MeV linac we have a chicane-type compressor for upward chirping.

Bunch shapes obtained with and without bunch compression are shown in Fig. 3. The 13-ps bunch is compressed to 440 fs (FWHM). The best pulse compression was done around the phase of the best emittance. After this measurement, we calibrated the streak camera by using an 86-fs (FWHM) Ti:sapphire laser (Spectra-Physics, Tsunami). The 86-fs laser pulse was elongated to 390 fs. Thus, according to the error propagation law, the error at the camera was estimated to be 370 fs (FWHM). We found that this error was mainly due to the degradation of the microchannel plate (MCP) in the streak tube. If we assume independent Gaussian distributions for both the electron bunch and the error, the error propagation law gives a bunch length of 240 fs (FWHM) after the error reduction. When we do not assume that the distributions are Gaussian and use the error propagation function evaluated from all measured data, the bunch length becomes 290 fs (FWHM). After this experiment, we replaced the degraded MCP with a new one, the error of which has been evaluated by the same procedure to be 240 fs.[12]

4. Pulse shape diagnosis

a. Femtosecond streak camera

We have used a commercial femtosecond streak camera (FESCA200, Hamamatsu Photonics, Japan) with a time resolution of 200 fs (FWHM). We measure electron pulse shape via Cherenkov radiation in air and Xe gas for more and less than 20 MeV electrons, respectively. If a focusing lens is used, the optical dispersion and wide spectrum of the Cherenkov radiation yield serious pulse elongation. We therefore instead use a narrow(about 10 nm) bandpass filter. But this reduces the radiation intensity at the camera so much that the signal-to-noise ratio becomes poor.[14] To solve this problem we constructed a non-dispersive optics using only reflective mirrors to guide the radiation. This improved the signal-to-noise ratio remarkably, maintaining the time resolution even when a 20-nm filter was used.[15]

b. Coherent radiation interferometer

When an electron bunch passes through the interface of two media of different dielectric constants, it emits transition radiation (TR)

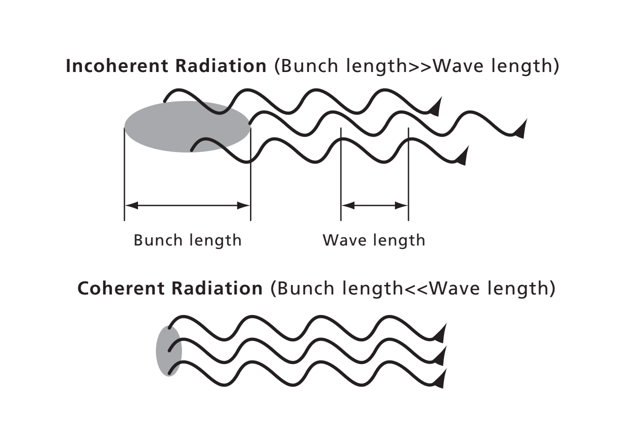

Fig.4 Incoherent / Coherent radiation

that carries the information of the bunch distribution. Similarly, when an electron bunch passes through an aperture in a dielectric material or near the edge of a dielectric material, diffraction radiation (DR) is emitted from the edge. The relation between the transition radiation $I_{e,TR}$ and the diffraction radiation $I_{e,DR}$ is given by the following equation:[16)]

$$I_{e,DR}(D,\nu,\theta)=I_{e,TR}(\nu,\theta)[E(D,\nu,\theta)]^2 \tag{1}$$

where

$$E(D,\nu,\theta)=J_0(\pi\nu D\sin\theta)[\pi\nu D/(\beta\gamma)]K_1(\pi\nu D/(\beta\gamma)). \tag{2}$$

Here J_0 is the 0th-order Bessel function, D is the diameter of an aperture, K_1 is the 1st modified Bessel function, ν is the wave number, θ is the radiation angle, and $\beta\gamma$ are the relativistic factor of the electron. The diffraction radiation due to an infinitesimal hole ($D \approx 0$) corresponds to the transition radiation.

When the wavelength of the radiation is shorter than the length of the electron bunch, the radiation is incoherent because the phase of the radiation emitted by one electron differs from that of the radiation emitted by another electron. And as shown in Fig. 4, when the wavelength is longer than the bunch length, the radiation is almost coherent because the phase of the radiation by any electron is almost as that of the radiation emitted by the others. This results in the temporal coherence of radiation. Coherent radiation yields an interferogram when we use an interferometer such as the Michelson interferometer, and the information in the electron bunch can be inferred from the interferogram. Another important feature of coherent radiation is the dependence of the power on the number of electrons in the bunch. The following equations show that the power of incoherent radiation increases linearly with the number of electrons while that of coherent radiation increases linearly with the square of the number of electrons. When two coherent radiation pulses interfere, the longitudinal bunch distribution can be derived from the interferogram of the light intensity by the following procedure.

When the cross section of the beam is small and the observation point is far from the source, the intensity of the transition radiation is expressed — by analogy to the intensity of coherent synchrotron radiation — as[16,17,18)]

$$I(\nu)=N[1+(N-1)f(\nu)]I_e(\nu) \tag{3}$$

where N is the number of electrons in the bunch, ν is the wave number (the inverse of the wavelength of the transition radiation) and $I_e(\nu)$ is the intensity of the transition radiation emitted by a single electron. The first term of Eq. (3) represents the incoherent transition radiation and the second term represents the coherent transition radiation. The quantity $f(\nu)$ is the bunch form factor, which is given by the Fourier transform of the distribution function, $S(\vec{x})$, of electrons in the bunch:

$$f(\nu)=\left|\int S(\vec{x})\exp[i2\pi(\vec{n}\cdot\vec{x})\nu]d\vec{x}\right|^2 \tag{4}$$

where $\vec{n}$ is the unit vector directed from the center of the bunch to the observation point and $\vec{x}$ is the position vector of the electron relative to the bunch center. Since $N>>1$,

$$I_{total}\approx N^2 f(\nu)I_e(\nu). \tag{5}$$

The form factor $f(\nu)$ can be divided into two parts, the longitudinal bunch form factor $f_L(\nu)$ and the transverse bunch form factor $f_T(\nu)$, as follows:[18)]

$$f(\nu)=f_L(\nu)f_T(\nu) \tag{6}$$

where

$$f_L(\nu)=\left|\int_{-\infty}^{\infty}h(z)exp(i2\pi z\cos\theta/\nu)dz\right|^2 \tag{7}$$

$$f_T(\nu)=\left|2\pi\int_0^{\infty}g(\rho)J_0(2\pi\rho\sin\theta\nu)\rho d\rho\right|^2. \tag{8}$$

Here $h(z)$ and $g(\rho)$ are respectively the longitudinal and transverse distribution functions of the electron bunch, and we assume that the transverse beam distribution is circular. The transverse bunch form factor is obtained by measuring the transverse distribution of the electron bunch. When we observe the transi-

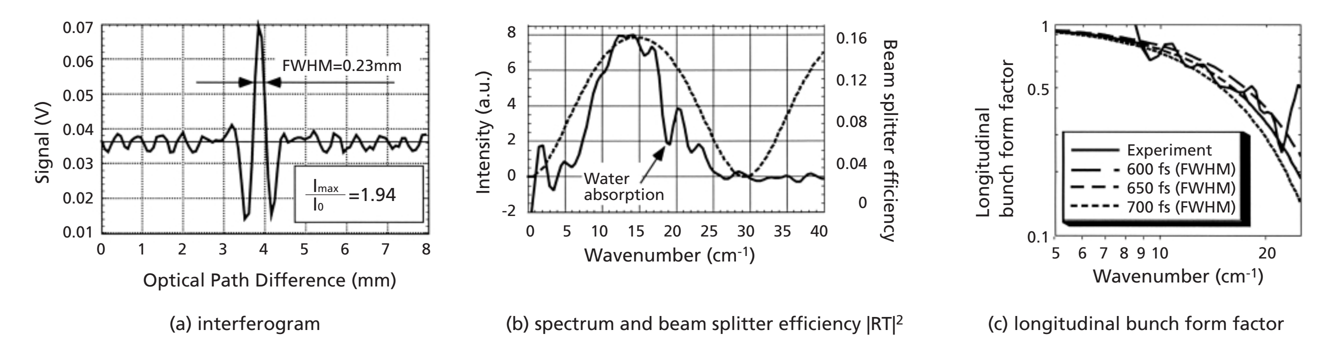

Fig.5 Interferogram, spectrum and longitudinal bunch form factor of subpicosecond electron pulse by CTR interferometry.

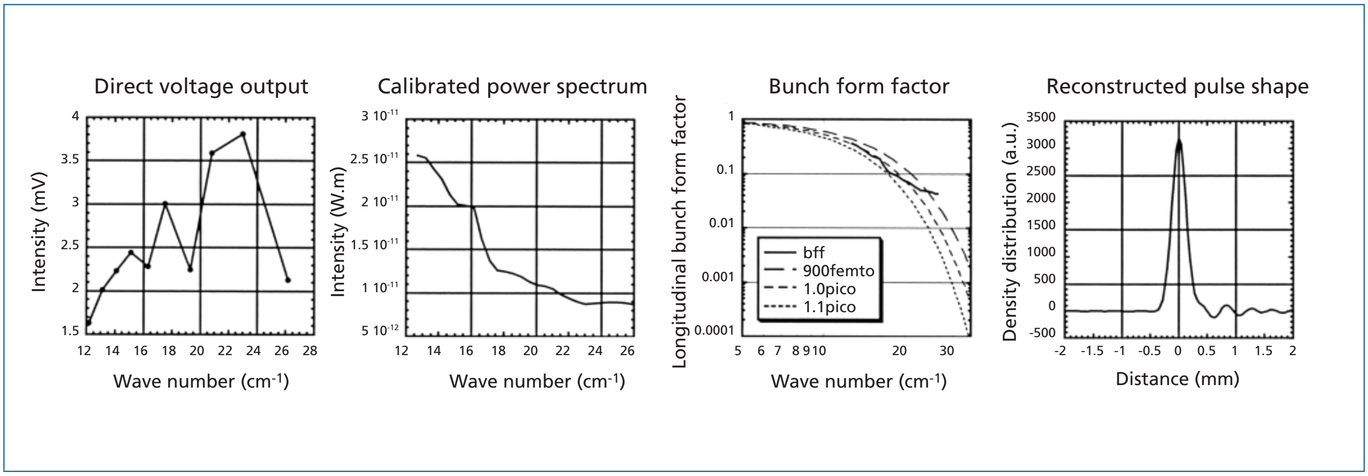

Fig.6 Reconstruction of subpicosecond electron pulse by the polychromator

tion radiation from an on-axis or nearly on-axis direction (i.e., θ^2>>1), cos θ and sin θ can respectively be unity and zero. Equations (7) and (8) can then be rewritten approximately:

$$f_L(\nu)=\left|\int_{-\infty}^{\infty} h(z)exp(i2\pi z)dz\right|^2 \equiv \left|F_L(\nu)\right|^2 \qquad (9)$$

and

$$f_T(\nu)=\left|2\pi\int_0^{\infty} g(\rho)J_0(0)\rho d\rho\right|^2 \qquad (10)$$

where $F_L(\nu)$ is the Fourier transform of the longitudinal bunch distribution $h(z)$, $g(\rho)$ is the transverse bunch distribution, and $J_0(0)$ is the 0th-order Bessel function.

The interferogram of the light intensity of two interfering coherent transition radiation pulses as a function of the position of the movable mirror of the Michelson interferometer is obtained as shown in Fig. 5(a). The interferogram can be written

$$S(\delta)=4\pi\int_{-\infty}^{\infty}|RT|^2\left|\tilde{E}(\nu)\right|^2 e^{-i2\pi\nu\delta/c}d\nu \qquad (11)$$

where $S(\delta)$ is the intensity of the recombined radiation intensity at the detector (expressed in the time domain with an additional time delay δ/c for the movable mirror) minus the intensity at $\delta\rightarrow\pm\infty$, $\tilde{E}(\nu)$ is the Fourier transform of the electrical field of the transition radiation, and R and T are the coefficients of reflection and transmission at the beam splitter.

Solving for $|\tilde{E}(\nu)|^2$ yields

$$\left|\tilde{E}(\nu)\right|^2=\frac{1}{4\pi c|RT|^2}\int_{-\infty}^{\infty}S(\delta)e^{-i2\pi\nu\delta/c}d\delta. \qquad (12)$$

The spectrum deduced from the interferogram is shown in Fig. 5(b), where the theoretical beam splitter efficiency is also drawn in order to show non-uniform sensitivity for wave numbers. This effect is compensated by using the theoretical curve.

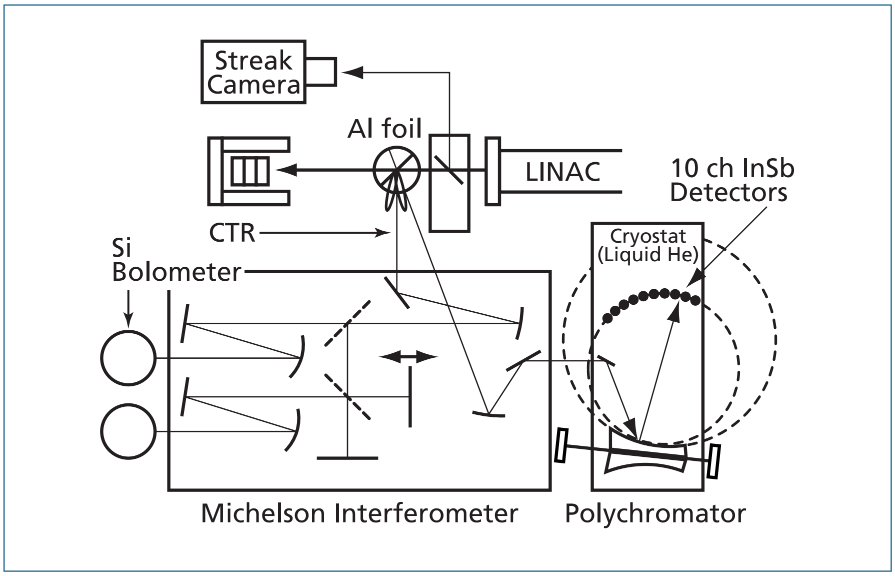

Fig.7 Measurement setup for the femtosecond streak camera, CTR interferometer and polychromator.

Using Eq. (5) and the relation $I_{total}(\nu)=|\tilde{E}(\nu)|^2$, we can obtain the following equation for the bunch form factor:

$$f(\nu)=\frac{\int_{-\infty}^{\infty}S(\delta)e^{-i2\pi\nu\delta/c}d\delta,}{4\pi c|RT|^2N^2I_e(\nu)}. \qquad (13)$$

Then, as is seen in Fig. 5(c), the longitudinal bunch form factor is obtained using Eqs. (6) and (13). Finally, the Kramers-Kronig relations and inverse Fourier transform give the longitudinal bunch distribution $h(z)$ from the longitudinal bunch form factor as follows:[16,18)]

$$f(z)=\int_{-\infty}^{\infty}g(\nu)\exp[i(\phi_g(\nu)-2\pi\nu t)]d\nu \qquad (14)$$

$$g(\nu)=f_L^{1/2}(\nu) \qquad (15)$$

$$\phi_g(\nu)=\pm2\nu\int_0^{\infty}\frac{\ln[g(\nu')/g(\nu)]}{\nu'^2-\nu^2}d\nu'. \qquad (16)$$

c. Far-infrared polychromator

By using the polychromator, the spectrum of the radiation can be obtained directly from the frequency measurement bins of the output voltage as shown in Fig. 6.[15,19)] Then the bunch distribution can be deduced by the same procedure used in interferometry. One can skip the procedure to get the spectrum described as Eq. (12). This simplification of the analysis is one of the advantages of the polychromator method. Another important advantage is that it can be used to diagnose the electron bunch by a single shot. The spectral information obtained in an experiment, however, is limited by the number of detectors. The typical output voltage of the polychromator is shown on the left-hand side of Fig. 6. The response function of the optics and the sensitivity of the detector in each channel of the polychromator were calibrated using the mercury arc as well as the interferometer. Furthermore, the discreteness of the experimental data, which depends on the grating pitch and the configuration of the measurement bins installed in the polychromator, is interpolated in order to obtain a continuous spectrum.

d. Performance

The experimental setup is shown in Fig. 7. The incoherent Cherenkov radiation emitted in air was measured by the streak camera, and the CTR in the far-infrared region was measured by the Michelson interferometer and the polychromator. At the Michelson interferometer the radiation was split into two bunches at a beam splitter and, after one bunch was delayed by the linear stage, the two bunches were recombined at the same beam splitter and the resulting signal was detected by a Si bolometer cooled in liquid helium. The radiation, which is transported to the polychromator, is deflected by the grating and then resolved by the 10-channel-detector array. The polychromator, which was constructed by Y. Kondo et al.,[19] covers wave numbers from 12.2 to 26.2 cm^{-1}. When the mirror mounted on the motorized linear stage was moved to the beam path at the linac exit, Cherenkov radiation emitted in air was transported to the streak camera. The major beam parameters were as follows: the electron energy was 34 MeV, and the electron charge per bunch was controlled between 10 and 100 pC to keep the detectors from saturating. The bunch length was adjusted to be about 900 fs (FWHM, or 380 fs rms) and 1.6 ps (FWHM, 680 fs in rms) at the linac by using the streak camera.

Consequently, the longitudinal bunch distribution was inferred from information provided by the streak camera, the Michelson interferometer, and the polychromator (Fig. 8). This is the first time agreement among the three methods has been shown for a roughly 1-ps electron bunch.

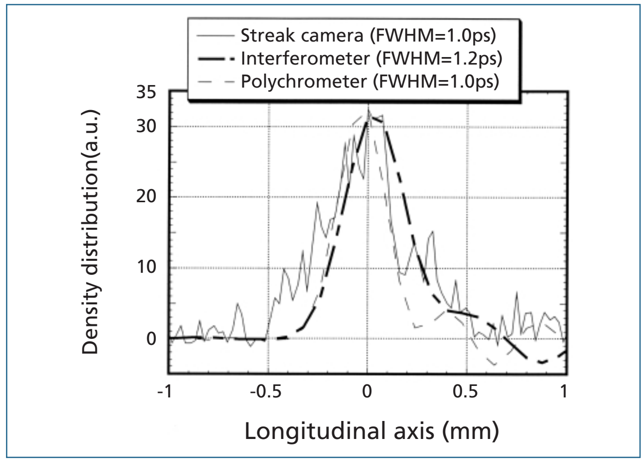

Fig.8 Measured electron pulse shape by the femtosecond streak camera, CTR interferometer and polychromator.

e. Fluctuation method

When the wavelength of the radiation is shorter than the length of the electron bunch, the random phase of the radiation emitted from a single electron, $E_0(t)$, causes the total electric field $E(t)$ in a bunch to fluctuate randomly: [20]

$$E(t)=\sum_{j}^{N}E_0(t-t_j). \tag{17}$$

A photodiode can measure only the time-integrated intensity $\int|E(t)|^2dt$, and shot-by-shot fluctuations in the radiation are eventually obtained in the experiment. As pointed out in Ref. 20, the fluctuation of the time-integrated intensity gives information about the number of independent parts in a bunch, N_{indep}. One can write

$$\sigma^2=\frac{F}{N_{indep}}=\frac{F\tau_{coh}}{\tau_b}, \tag{18}$$

where F is a form factor that is computed from the Fourier transform of the bunch distribution, and τ_{coh} and τ_b are respectively the durations of the independent part and the bunch. The duration of the independent part, τ_{coh}, which is associated to the coherent time, results from the finite length of the envelope of the electric field emitted by a single electron and it can therefore be calculated from the bandwidth of the radiation.

We first measured the time-integrated intensity of the incoherent radiation in several bandwidths. The experimental setup is shown in Fig. 9(a). Cherenkov radiation emitted in air was measured with optical transition radiation (OTR). OTR, however, is much less intense than Cherenkov radiation, so the influence of OTR can be ignored. In the experiment the spectrum was limited by the bandpass filter so that the coherent time would be a fraction of the bunch duration. The calculated intensities of electric field of incoherent radiation with and without the bandpass filter are shown in Figs. 9(b) and 9(c). As is seen from the figures, by introducing the band pass filter, the electric field is made of about ten independent spikes, each of which has a random amplitude. Figure 10 shows the fluctuation of time-integrated intensity, where the measured pulse width was 1.0 ps by the streak camera.[21] However, by the measured fluctuation the pulse width was estimated to be 4.5 ps. The discrepancy between the above results was due to the transverse beam size of the bunch, since so far we have

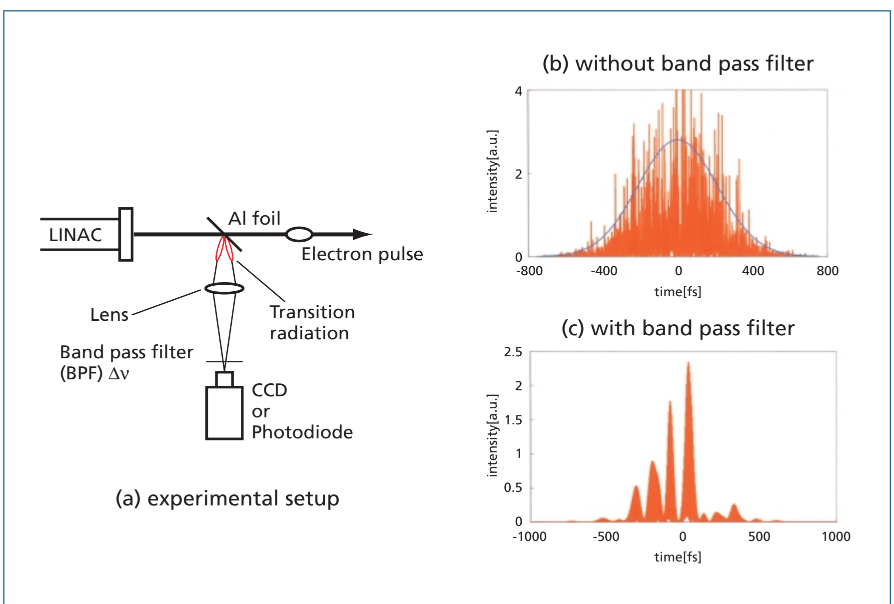

Fig.9 Measurement setup and numerical results of pulse structure for the fluctuation method.

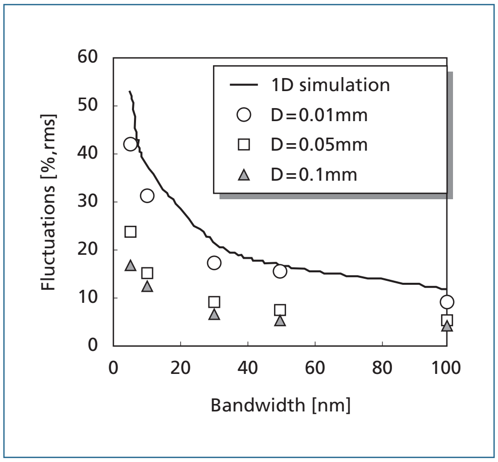

Fig.10 Fluctuation of radiation power at several bundpass filters.

Table 1 Overall comparison of the four diagnostic methods

	Radiation	Single shot	Time resolution	Influence of other parameters	Dynamic range	Timing jitter evaluation
Streak camera	Incoherent Low intensity	available	200fs	small	wide	available
Interferometer	Coherent High intensity	not available	theoretically unlimited	large	relatively narrow	not available
Polychromator	Coherent High intensity	available	theoretically unlimited	large	relatively narrow	not available
Fluctuation	Incoherent Low intensity	available	theoretically unlimited	relatively small	relatively wide	not available

assumed that the transverse beam size is infinitesimal. It is worth noting that an infinitesimal transverse beam diameter is assumed in the above theory, whereas the transverse beam diameter in our experiment was more than 1 mm and cannot be ignored. To increase the precision of our work, we are now using two-dimensional numerical analysis to take into account the effect of the transverse beam size on the fluctuation. The transverse beam size at the radiation sources was measured to be 3 mm (FWHM of Gaussian distribution) for a 1.0-ps pulse width.

The spectrum shows fluctuation shot by shot. It is known that observation of the spectrum provides more information than does observation of the time-integrated power.[22] The longitudinal bunch distribution can be inferred by analyzing the variance of the Fourier transform of the spectrum, and information about the transverse beam size can also be extracted from the spectrum. It is therefore expected that the pulse information will be obtained in the frequency-domain measurements that are under way.

f. Overall Evaluation

For pulse widths up to 200 fs, it is obvious that the streak camera is the best. As for less than 200 fs, upgrade, combination and crosscheck among the other methods are needed. Shot-by-shot measurement is available for the streak camera and polychromator and is important for evaluating the beam stability. The timing jitter between two pulses, which determines the time resolution of pump-and-probe analysis, can be evaluated only by the streak camera. The overall evaluation of our instruments and methodology is summarized in Table. 1.

5. Laser plasma cathode for tens-of-femtosecond electron single bunch generation

a. Pump-and-probe analysis using femtosecond beams

Here we introduce the generation of ultrashort-bunched electron beams from underdense plasma driven by ultrashort and ultra-intense laser pulses. For this purpose, computer simulations and experiments based on the 12-terawatt 50-fs laser system have been conducted.

The target short electron bunch along with the short laser pulses already available could be used to make a pump-and-probe system for studying, for example, the initial phase of radiation-induced chemical reactions. A proposed configuration for such application is shown in Fig. 11. A beam splitter would be used to split the 12-TW 50-fs laser beam into an intense beam (≈11.5 TW) used for electron beam generation and a less intense beam (≈0.5 TW) used as a probe.

b. Laser wakefield accelerator

Of particular interest in the laser plasma acceleration schemes is the laser wakefield accelerator (LWFA),[23] in which an intense laser pulse propagates through underdense plasma and generates large-amplitude plasma waves (wakefields) by the effect of the ponderomotive force associated with the laser pulse envelope. A plasma density n_o of 10^{18} cm^{-3} can support a field E_0 of 100 GV/m. The plasma wavelength of interest is of the

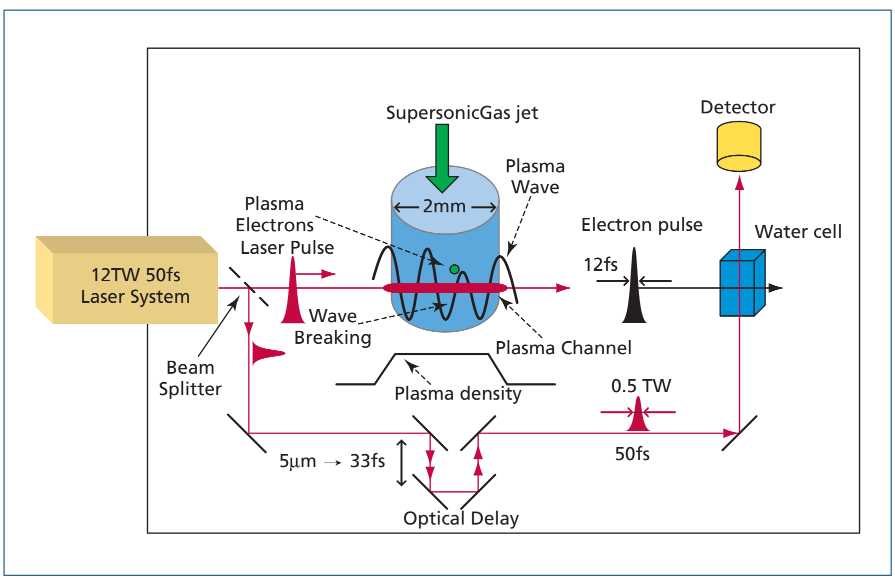

Fig.11 Schematic diagram of a pulse radiolysis system based on femtosecond bunched electron beam generated from an ultraintense ultrashort laser-plasma interaction.

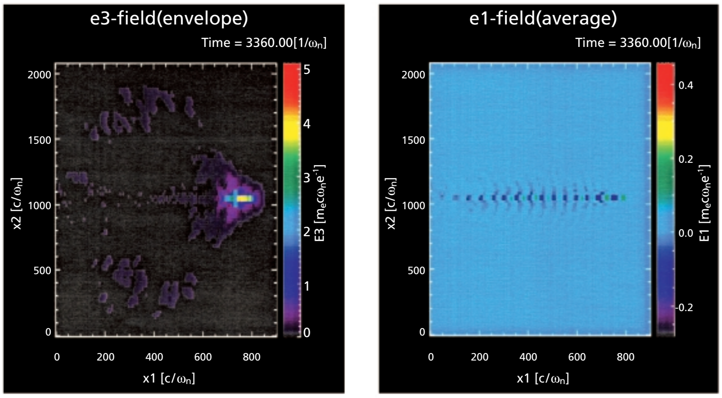

Fig.12 The 2D-PIC computer simulations (a) The contour plot of the laser pulse as it propagates through underdense plasma. The laser is self-focused (b) The plasma wave generated behind the laser pulse.

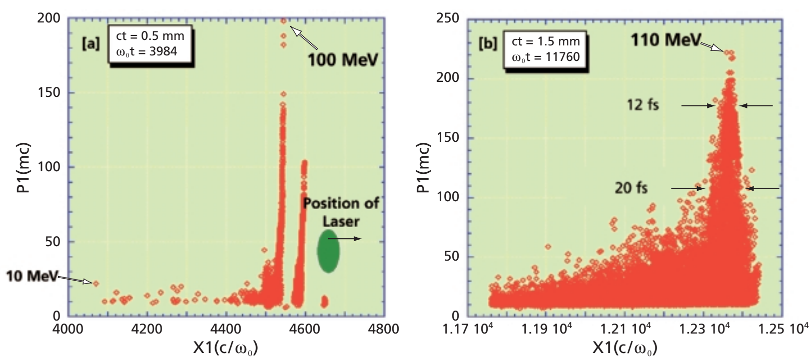

Fig.13 The 2D-PIC computer simulations. The longitudinal phase space of the trapped and accelerated plasma electrons after the laser pulse has propagated (a) 0.5 mm through the plasma. (b) 1.5 mm through the plasma.

order of 10-100 μm, so the longitudinal length of the accelerated and/or injected (for additional acceleration) electron bunches should be within this range. Furthermore, the electron bunch should be injected in the correct phase in order to get trapped and accelerated by the wave. Two schemes based on laser-triggered electron trapping in the plasma wave has been proposed for generating ultrashort electron beams.[24] For this purpose, several laser pulses should be synchronized in space and time more precisely than currently possible. We have therefore proposed[25] a system based on the use of a single ultra-intense laser pulse focused in the plasma (Fig. 11).

The basic idea for generating the electron bunch is to trap and accelerate some of the plasma electrons in a nonlinear plasma wave, which is forced to 'break' in the plasma. At the wave-breaking region, many ultrashort-bunched electrons are accelerated and leave the plasma with relativistic energies.

c. Simulations

Two-dimensional (2D) simulations were done using the recently developed fully relativistic particle-in-cell code OSIRIS.[26] The simulations for the gas jet 1.5 mm in diameter were run for a time of 12600 ω_L^{-1}(ω_L is the laser frequency), that is 4.6ps. We set the maximum plasma density to 5×10^{19}/cm^3 and the laser pulse as 12-TW 50-fs with spot size of 10 μm.

Figure 12 shows part of the 2D-PIC computer simulation results. Figure 12 (a) shows the contour plot of the laser pulse as it propagates through the plasma; the laser is self-focused. Figure 12(b) shows the contour plasma wave electric field generated behind the laser pulse. The laser intensity was originally 1.1×10^{19} W/cm^2 and reached 14.2×10^{19} W/cm^2 because of the self-focusing effect. The maximum amplitude of the electric field of the plasma wave,E_z, reached 0.7 TV/m. The self-focusing of the laser and the generation of super-high electric field in the plasma wave are essential in the process of electron trapping and acceleration as will be made clear below. Figure 13 shows the longitudinal phase-space of plasma electrons trapped and accelerated to 110 MeV by the plasma waves. A plasma-wavebreaking mechanism for producing for a sharp density gradient when electrons are injected into the plasma waves has been proposed, [27] but for a laser pulse of relativistic intensity ($a = eE_L / m\omega_L c > 1$), the electron injection (regardless of how sharp the density gradients are) is based on the breaking of waves produced by the relativistic acceleration of electrons into wakefield waves. The relativistic force, which acts along the laser propagation direction, grows as a^2.[28] As shown in Fig. 13(a), the relativistic force creates waves with wavelengths of the order of the laser wavelength propagating with the laser pulse. The maximum energy of electrons in the waves is determined by the longitudinal component of the electron momentum:

$$\gamma = \frac{P_x}{mc} = \frac{a^2}{2}\sin^2(\omega t + kx). \tag{19}$$

These electrons constitute the injection source for the following relativistic wave so that electrons acquire the maximum energy after propagating 0.5 mm as shown in Fig. 13(a) or after propagating 1.5 mm as shown in Fig. 13(b).

We can see in Fig. 13(b) that the average energy of all electrons is 22.5 MeV, but an energy spread of 100 % was produced. Using a magnetic chicane, it is possible to filter this beam in order to get a beam with a smaller energy spread. In the energy range from 82 MeV to 110 MeV, the bunch length was 3.5μm (equivalent to ≈12 fs), the rms emittance was ≈0.7 mm mrad, and the total charge of accelerated electrons was about 580 pC.

d. Experiment

The experiment was performed with the 12-TW laser system that delivers 600-mJ 50-fs pulses at 790 nm. The laser beam was focused with an f/2 off-axis parabolic mirror to a spot about 20 µm in diameter. The peak intensity in the focus point is expected to exceed 10^{19} W/cm^2. The focus was placed at the edge of a free-expansion helium gas jet generated by a high-pressure gas nozzle with a circular orifice 2 mm in diameter. The density profile has been measured by Mach-Zehnder interferometry. The transverse density profile in the interaction region 2 mm above the nozzle tip corresponds to a Gaussian profile. The electron density in the tunnel-ionized underdense plasma created by the foot of the laser pulse is, up to a maximum value of 5×10^{20} /cm^3, linearly proportional to the backing pressure.

The transverse profile image of the electron beam observed when the laser power and plasma density were 4 TW and 2.7×10^{20} / cm^3 is shown in Figure 14. Such beam has been observed at a distance of 20 cm after the gas jet inside the experimental vacuum chamber. A thin foil of aluminum was inserted after the gas jet to prevent the laser light from reaching the electron beam detection system. The angle of divergence of the electron beam was about 120 mrad. Since the diameter of the beam was about 10 microns at the focus point, the total beam emittance was about 4 π mm mrad. The charge of the electron beam was measured by using a Faraday cup outside the vacuum chamber. The total charge measured within an angle of 70 mrad was 14 pC. It should be noted that this measurement underestimates the beam charge because of the limitation due to the limited collection angle. Further measurements to verify about 10fs electron pulse are planned.

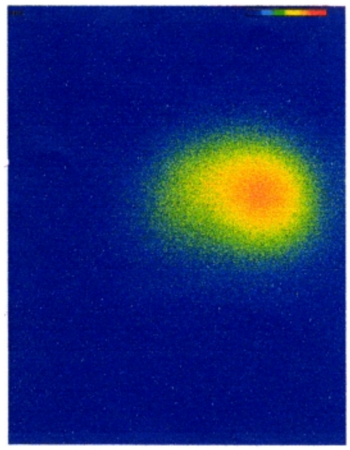

Fig.14 The transverse profile of the electron beam observed in the intense laser plasma interaction. The laser power was 4 TW and the plasma density was 2.7×10^{20}/ cm^3.

Conclusion

We introduced sophisticated technologies for generating and diagnosing ultrashort electron beams, which enables a pump-and-probe analysis to investigate ultrafast microscopic dynamics in matters. These technologies are under development at the University of Tokyo's Nuclear Engineering Research Laboratory, where we are leaders in the race to "dynamic nanotechnology." We hope these technologies will help establish a major new scientific field in the 21st century. JSAP

Reference

1) P. Kung, Hung-chi Lihn, and Helmut Wiedemann: Phys. Rev. Lett. **73**, 967-970 (1994).
2) M. Uesaka, K. Tauchi, T. Kozawa, T. Kobayashi, T. Ueda, and K. Miya: Phys. Rev. E **50**, 3068-3076 (1994).
3) X. J. Wang, X. Qiu, and I. Ben-Zvi: Phys. Rev. E54, R3121-3124(1996).
4) Y. Liu, X. J. Wang, D. B. Cline, M. Babzien, J. M. Fang, J. Gallardo, K. Kusche, I. Pogorelsky, J. Skaritka, and A. van Steenbergen: Phys. Rev. Lett. 80, 4418-4421(1997).
5) http://www-ssrl.slac.stanford.edu/lcls
6) http://tesla.desy.de/new-pages/4000_TTF-project.html
7) I. V. Pogorelsky, I. Ben-Zvi, T. Hirose, S. Kashiwagi, V. Yakimenko, K. Kusche, P. Siddons, J. Skaritka, T. Kumita, A. Tsunemi, T. Omori, J. Urakawa, M. Washio, K. Yokoya, T. Okugi, Y. Liu, P. He, and D. Cline: Phys. Rev. Special Topics - Accelerators and Beams **3**, 090702-1-8 (2000).
8) J. F. Wishart: Accelerator for Ultrafast Phenomena, in *Radiation Chemistry: Present Status and Future Trends* (Studies in Physics and Theoretical Chemistry **87**), ed. C. D. Jonah and B. S. M. Rao, Elsevier Science, Amsterdam, 21-35 (2001).
9) T. Kozawa, Y. Mizutani, M. Miki, Y. Yamamoto, S. Suemine, Y. Yoshida, and S. Tagawa: Nucl. Instrum. Methods A **440**, 251-253 (2000).
10) Y. Muroya, T. Watanabe, G. Wu, X. Li, T. Kobayashi, J. Sugahara, T. Ueda, K. Yoshii, M. Uesaka, and Y. Katsumura: Radiation Physics and Chemistry **60**, 307-312 (2001).
11) M. Uesaka, T. Watanabe, T. Kobayashi, T. Ueda, K. Yoshii, X. Li, Y. Muroya, J. Sugahara, K. Kinoshita, N. Hafz, and H. Okuda: Radiation Physics and Chemistry **60**, 303-306 (2001).
12) M. Uesaka, K. Kinoshita, T. Watanabe, J. Sugahara, T. Ueda, K. Yoshii, T. Kobayashi, N. Hafz, K. Nakajima, F. Sakai, M. Kando, H. Dewa, H. Kotaki, and S. Kondo: Trans. Plasma Science **28**, 1133-1142 (2000).
13) T. Kobayashi, M. Uesaka, Y. Katsumura, Y. Muroya, T. Watanabe, T. Ueda, K. Yoshii, K. Nakajima, X. Zhu, and M. Kando: J. Nucl. Sci. Technol. (2001). in press
14) M. Uesaka, T. Ueda, T. Kozawa, and T. Kobayashi: Nucl. Instrum. Methods **406**, 371-379 (1998).
15) T. Watanabe, J. Sugahara, K. Yoshii, T. Ueda, M. Uesaka, Y. Kondo, T. Yoshimatsu, Y. Shibata, K. Ishii, S. Sasaki, and Y. Sugiyama: Nucl. Instrum. Methods A. (2000). in press
16) Y. Shibata, K. Ishii, T. Takahashi, F. Arai, M. Ikezawa, K. Takami, T. Matsuyama, K. Kobayashi, and Y. Fujita: Phys. Rev. A **44**, 3449-3451 (1991).
17) T. Watanabe, M. Uesaka, J. Sugahara, T. Ueda, K. Yoshii, Y. Shibata, F. Sakai, S. Kondo, M. Kando, H. Kotaki, and K. Nakajima: Nucl. Instrum. Methods A **437**, 1-11 (1999).
18) R. Lai and A. J. Sievers: Phys. Rev. E **50**, 3342-3344 (1994).
19) J. Sugahara, T. Watanabe, K. Yoshii, T. Ueda, M. Uesaka, Y. Kondo, Y. Shibata, and M. Ikezawa: Proceedings of Particle Accelerator Conference (New York, USA), 2871-2873 (1999).
20) M. S. Zolotorev and G.V. Stupakov: Proceedings of Particle Accelerator Conference (Vancouver, Canada), 2180-2182 (1998).
21) T. Watanabe, K. Nakamura, T. Ueda, and M. Uesaka: Proceedings of Particle Accelerator Conference, Chicago, USA (2001). in press
22) P. Catravas, W. P. Leemans, J. S. Wurtele, M. S. Zolotorev, M. Babzien, I. Ben-Zvi, Z. Segalov, X. J. Wang, and V. Yakimenko: Phys. Rev. Lett. **82**, 5261-5264 (1999).
23) E. Esarey, P. Sprangle, J. Krall, and A. Ting: IEEE Trans. Plasma Sci. **24**, 252-288 (1996).
24) D. Umstadter, J. K. Kim, and E. Dodd: Phys. Rev. Lett. **76**, 2073-2076 (1996) and E. Esarey, R. F. Hubbard, W. P. Leemans, A. Ting, and P. Sprangle: Phys. Rev. Lett. **79**, 2682-2685 (1997).
25) N. Hafz, J. Koga, M. Uesaka, and K. Nakajima: Nucl. Instrum. Methods A **455**, 148-154 (2000).
26) R. Hemker: Ph.D. thesis, University of California, Los Angeles (2000).
27) S. Bulanov, N. Naumava, F. Pegoraro, and J. Sakai: Phys. Rev. E **58**, 5257-5260 (1998).
28) A. Zhidkov, A. Sasaki, and T. Utsumi: Phys. Rev. E **62**, 7232-7240 (2000).